High-performance three-body near-field thermophotovoltaic energy conversion

Chunzhuo Dang[a], Xianglei Liu[a,*], Haifeng Xia[b], Shizheng Wen[a], Qiao Xu[a]

[a] School of Energy and Power Engineering, Nanjing University of Aeronautics and Astronautics, Nanjing 210016, China
[b] Hengli Eletek Co., Ltd., China

ARTICLE INFO

ABSTRACT

Three-body structures have shown great potentials in enhancing the heat transfer rate and tuning radiation spectrum in the near-field region, whereas are rarely considered in improving near-field radiative energy conversion performance. Here, a three-body thermophotovoltaic system configured by a tungsten emitter, a metallic spectrum control layer, and an $In_{0.18}Sb_{0.82}Ga$ photovoltaic cell is considered. By parameter optimization of the spectrum control layer, the efficiency and output power at the gap distance of 10 nm are enhanced from 24.7% and 1.88×10^5 W/m^2 to 35.3% and 3.62×10^5 W/m^2, respectively. The potential mechanism lies in the excitation of coupled surface plasmon polaritons of the metallic spectrum control layer. This work paves the way for applications of three-body structure in thermophotovoltaic systems and designing high-performance energy conversion systems.

© 2020 Elsevier Ltd. All rights reserved.

1. Introduction

Ever-increasing energy demands require proper solutions to harvest enormous waste thermal energy in industry [1,2]. The thermoelectric generator is the most widely used solid-state heat-to-electricity technique for this purpose but suffers from low efficiency [3]. As an alternative approach, the thermophotovoltaic (TPV) system is promising to achieve a higher efficiency [1,4]. A TPV system is usually composed of a high-temperature emitter and a photovoltaic cell receiver with a low temperature. The photovoltaic cell receives thermal radiation from the emitter and converts it into electrical energy [5]. Since the TPV system can utilize different heat sources, it's versatile in applications such as solar energy collection and waste heat recovery [6,7]. Possessing desirable features including simple components, no moving parts, and compact structures, TPV systems have got intense attention in recent years [5,6,8-15]. Despite all that, one bottleneck challenge of the TPV system is its low output power, restricted by the blackbody radiation limitation [14].

Fortunately, people have found that when the gap distance between the thermal emitter and the photovoltaic cell is reduced below the value of characteristic wavelengths, the radiative heat flux can far exceed the blackbody radiation limit [16-27]. Many theoretical [2,5,17,28-41] and experimental efforts [42-45] have

been conducted to investigate near-field TPV systems. Especially, recently, by employing thin films, graphene layers, hyperbolic materials, gratings, etc. [2,5,29,33-36,46-50], people have successfully improved the performance of the near-field TPV system. For example, Bright et al. proposed a receiver composed of a thin film cell and a backside gold mirror, this structure's efficiency enhancement reached the level of 35% compared to a semi-infinite cell [2]. Watjen et al. applied an optimized tungsten grating to replace a flat tungsten emitter, and an increase of 6% in efficiency has been theoretically demonstrated [5]. Nevertheless, compared with TPV systems' Carnot efficiency limit [6,14], the efficiency still has much room for improvement.

Recently, three-body structures have been employed to control near-field radiative heat transfer [51-60]. Zheng and Xuan first studied the effect of inserting an intermediate body on near-field radiative heat transfer properties between two objects [55]. They showed that inserting doped silicon films can enhance the radiative heat flux while aluminum films have a suppression effect. Messina et al. placed a passive relay amplifier between two SiC plates and observed better monochromaticity of the thermal radiation spectrum [51]. Inspired by these phenomena, we are wondering whether the three-body structure can be applied to enhance the performance of the near-field TPV system by tuning the radiation spectrum.

In this article, we propose a three-body near-field TPV system and study its radiative energy transfer and conversion performances. Dyadic green functions combined with fluctuation-

* Corresponding author.
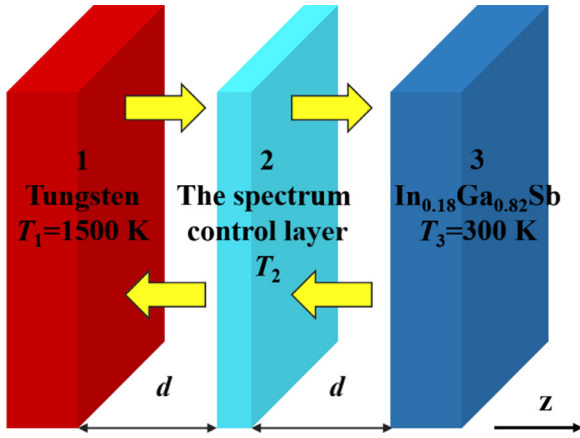   *E-mail address:* xliu@nuaa.edu.cn (X. Liu).

Fig. 1. Schematic of a three-body TPV system. The temperature of the spectrum control layer is determined based on energy balance.

dissipation theory are used to evaluate the energy transfer of three-body structures [7,61]. First, considering that the 1D photonic crystal filter has been applied to tune the thermal radiation spectrum in the far-field [9,10], we will study its performance as the spectrum control layer in near-field TPV system. Then, a thin metallic layer, whose dielectric functions are described by the simple Drude model, is considered. Effects of dielectric function parameters and vacuum gap distances on the system performance are investigated in detail, and corresponding underlying mechanisms are revealed.

2. Methods

Fig. 1 shows the configuration of the proposed TPV system. The emitter is tungsten, and the receiver is a $In_{0.18}Sb_{0.82}Ga$ photovoltaic cell. An immediate spectrum control layer is inserted in the middle between the emitter and receiver with a vacuum gap of width d. Both the emitter and receiver are assumed to be semi-infinite and their temperatures are set as $T_1 = 1500$ K and $T_2 = 300$ K, respectively. Dielectric functions of tungsten and $In_{0.18}Sb_{0.82}Ga$ are obtained from references [62,63]. The whole system is assumed to extend infinitely in the plane perpendicular to the z-axis.

Essentially the Poynting vector denotes an energy flux, and its time-averaged form $\mathbf{S}(\mathbf{x}, \omega) = \frac{1}{2} \langle \text{Re}[\mathbf{E}(\mathbf{x}, \omega) \times \mathbf{H}^*(\mathbf{x}, \omega)] \rangle$ is used to calculate radiative heat transfer [5,17,61]. $\mathbf{E}(\mathbf{x}, \omega)$ and $\mathbf{H}(\mathbf{x}, \omega)$ is the electric and magnetic fields at $\mathbf{x}$, respectively. They are closely related to the source current at $\mathbf{x}'$ caused by the thermal motion of charge carriers [64]:

$$\begin{cases} \mathbf{E}(\mathbf{x}, \omega) = i\omega\mu_0 \int_V \bar{\bar{\mathbf{G}}}_e(\mathbf{x}, \mathbf{x}', \omega) \cdot \mathbf{j}(\mathbf{x}', \omega)d\mathbf{x}' \\ \mathbf{H}(\mathbf{x}, \omega) = \int_V \bar{\bar{\mathbf{G}}}_m(\mathbf{x}, \mathbf{x}', \omega) \cdot \mathbf{j}(\mathbf{x}', \omega)d\mathbf{x}' \end{cases} \quad (1)$$

$\bar{\bar{\mathbf{G}}}_e(\mathbf{x}, \mathbf{x}', \omega)$ and $\bar{\bar{\mathbf{G}}}_m(\mathbf{x}, \mathbf{x}', \omega)$ are the corresponding electric and magnetic dyadic Green's function, which convert the source current at $\mathbf{x}'$ to electric and magnetic fields at $\mathbf{x}$. The entire TPV system structure can be considered as a multilayer structure with five layers. Green's functions between the homogeneous layer s and homogeneous layer l can be obtained by referring references [65–68].

The spectral heat flux is written as $q_{s \to l}(\omega) = \frac{\Theta(\omega, T_s)}{\pi^2} \int_0^\infty \xi_{s,l}(\omega, \beta)\beta d\beta$ and $q_{s \to l}(\lambda) = q_{s \to l}(\omega) \cdot \omega/\lambda$ corresponding to $\mathbf{S}(\mathbf{x}, \omega)$. $\Theta(\omega, T_s)$ is the average energy of the Planck oscillator . $\xi_{s,l}(\omega, \beta) = \xi_{l,s}(\omega, \beta)$ is the transmission coefficient between s and l. β is the transverse wave vector in the plane perpendicular to the z-axis. The whole heat flux from the layer s to the layer l can be written as the integral of the spectral heat flux $q_{s \to l}(\lambda)$ over the wavelength $Q_{s \to l} = \int_0^\infty q_{s \to l}(\lambda)d\lambda$.

In a stable working state, the system should be in a dynamic thermal equilibrium. The energy radiated by the spectrum control layer to the rest of the system at any time should be equal to the heat absorbed by the spectrum control element, which can be written as the relationship $Q_{2 \to 1} + Q_{2 \to 3} = Q_{1 \to 2} + Q_{3 \to 2}$. We can assume a temperature T_2 for the immediate body and apply it to the equation $Q_{2 \to 1} + Q_{2 \to 3} = Q_{1 \to 2} + Q_{3 \to 2}$. Through iterative calculations, we can obtain the real T_2. Then we can calculate the real heat transfer between the emitter and receiver as:

$$P_R = Q_{1 \to 2} + Q_{1 \to 3} - Q_{2 \to 1} - Q_{3 \to 1} = Q_{1 \to 3} + Q_{2 \to 3} - Q_{3 \to 1} - Q_{3 \to 2} \quad (2)$$

where $Q_{1out} = Q_{1 \to 2} + Q_{1 \to 3} - Q_{2 \to 1} - Q_{3 \to 1}$ is the amount of heat radiated by the emitter and $Q_{3in} = Q_{1 \to 3} + Q_{2 \to 3} - Q_{3 \to 1} - Q_{3 \to 2}$ is the amount of heat absorbed by the receiver. Although they are equal, their corresponding radiation spectrums q_{1out} and q_{3in} are not necessarily the same due to the role of the middle layer. q_{3in} is directly related to the energy conversion occurring within the photovoltaic cell. It should be noted that when the spectrum control element has a multilayer structure, $Q_{2 \to l} = \sum_{a=1}^{n} Q_{2-a \to l}$, $Q_{s \to 2} = \sum_{a=1}^{n} Q_{s \to 2-a}$. Here a represents the sequence number of a layer in the spectrum control element, n is the total number of layers.

We adopt the standard method to model the $In_{0.18}Sb_{0.82}Ga$ PV cell. As an indirect bandgap material, the saturation current characteristics of the $In_{0.18}Sb_{0.82}Ga$ cell are controlled by minority carriers. Ignoring surface and bulk recombination, each photon reaching the photovoltaic cell with an energy higher than its energy gap E_g can generate a pair of electron-hole pairs. The electrical power P_{el} can be calculated by using methods mentioned in Refs. [17,69]:

$$P_{el} = J_{ph}V_{oc}\left[1 - \frac{1}{\ln(J_{ph}/J_0)}\right]\left\{1 - \frac{\ln\left[\ln\left(J_{ph}/J_0\right)\right]}{\ln\left(J_{ph}/J_0\right)}\right\} \quad (3)$$

where $J_{ph} = \frac{e}{hc0} \int_0^{\lambda g} \lambda q(\lambda)d\lambda$ is the photogenerated current, $J_0 = e(N_i^2/N_A\sqrt{D_e/\tau_e} + N_i^2/N_D\sqrt{D_h/\tau_h})$ is the saturation current (where e is the electron charge, N_i is the intrinsic carrier concentration, D_e and D_h represents diffusion constant of the electrons and the holes, respectively; τ_e and τ_h refers to the electron relaxation time and the hole relaxation time, respectively; N_A and N_D are the acceptor concentration and the donor concentration, respectively. These parameters for calculation can be found in Ref.[17]), $V_{oc} = (k_BT/e)\ln(J_{ph}/J_0 + 1)$ is the open-circuit voltage [70,71]. The conversion efficiency can be calculated as $\eta = P_{el}/P_R \times 100\%$.

3. Results and discussion

First of all, we consider employing one-dimensional (1D) photonic crystals (PhCs) as the spectrum control layer, which has shown great potential in improving TPV systems' efficiency in the far-field. The 1D PhCs we employ are composed of alternating layers of SiO_2 and Si. By adopting the 1D PhCs design method (photonic crystal theory), we can obtain an optimized $L/2H(LH)^4$ structure, and more details can be found in Ref. [9]. $\lambda_g = 2.22$ μm is the wavelength corresponding to the energy gap E_g, which is used to calculate the thickness of layers:$L(SiO_2)$: $t_1 = 0.495$ μm, $H(Si)$: $t_2 = 0.218$ μm. To verify its ability to improve efficiency, we draw the spectral heat transfer diagram at $d = 100$ μm as shown in Fig. 2. We figure out body 2's temperature T_2 is 592.3 K. Under this circumstance, inserting PhCs is found to improve the conversion efficiency from 21.4% to 23.5%. That is because these below-bandgap photons lie in the forbidden band of PhCs, thus most of them are reflected back to the emitter, contributing to the increase of energy conversion efficiency. On the other hand, 1D PhCs cause a decrease of output power from 5142.8 W/m^2 to 3782.4 W/m^2. Since
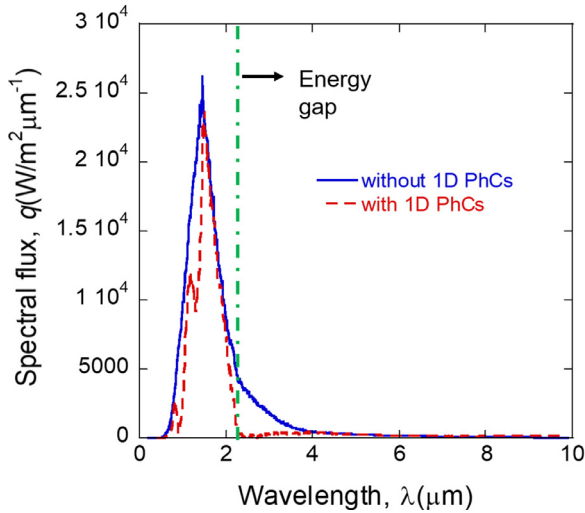
Fig. 2. Heat transfer spectrum of the TPV system at $d = 100$ μm. The blue curve and red dotted curve represents spectral flux arriving at the receiver for TPV systems without and with PhCs. The vertical green line represents bandgap at $\lambda = \lambda_g = 2.22$ μm.

Fig. 3. Conversion efficiency (a) and output power (b) of different TPV systems with gap distance d ranging from 10 nm to 100 μm. The temperature T_2 of the 1D PhCs filter is also plotted in **Fig. 3** (a).

the transmission of PhCs is not ideally 100%, the energy transfer of above-bandgap photons is inevitably deteriorated by the existence of PhCs, as shown in Fig. 2. That explains the lower output power after inserting the PhCs layer.

To check how inserting 1D PhCs affects the performance of near-field TPV systems, we calculate the efficiency and the output power of three-body TPV systems varying with the gap distance, as shown in Fig. 3. The conventional TPV system without any spectrum control layer with its emitter and receiver separated by the same gap distance of d is used for comparison. As we can see, when d is larger than 10 μm, the efficiency of both TPV systems becomes independent of the gap distance, which is the case of far-field. The three-body TPV system possesses higher efficiency and a lower output power due to 1D PhCs' filter effect. As the gap becomes smaller, the efficiency of both thermal photovoltaic systems began to decline after experiencing some fluctuations. Nevertheless, the efficiency of the three-body system is still higher than that of common TPV systems until when the gap further decreases below 150 nm. When the gap distance continuously decreases, efficiencies of TPV systems with and without PhCs demonstrate totally opposite trends. Inserting PhCs will heavily deteriorate the efficiency from 24.7% to 12.0% at $d = 10$ nm. The output power, on the other hand, tends to be always lower across the whole gap distance range after inserting the PhCs, as clearly shown in Fig. 3 (b). The temperature of spectrum control layer is around 600 K for the far-field case and has a quick increase to 1148.8 K when the gap distance decreases down to 10 nm. This trend is essentially determined by energy balance and will be explained later.

To explain why the efficiency of the three-body system deteriorates at nanoscale distances, we draw the spectral heat flux diagram at $d = 10$nm as shown in Fig. 4(a). Clearly, it can be seen that inserting PhCs inhibits the energy transfer of the three-body system for most wavelengths. Energy transmission coefficients for TPV systems without and with PhCs are given in Fig. 4(b) and Fig. 4(c), respectively. As can be seen clearly, the energy transmission coefficient decreases after inserting PhCs for most frequencies and wave-vectors, although the thee-body system is featured with lots of waveguide modes. Note that the rightmost SiO_2 layer may excite surface phonon polaritons as can be seen in the bottom bright region of Fig. 4(c). This helps improve heat transfer tremendously at the low-frequency region [72]. That's the reason why the spectral heat transfer of the three-body system is even
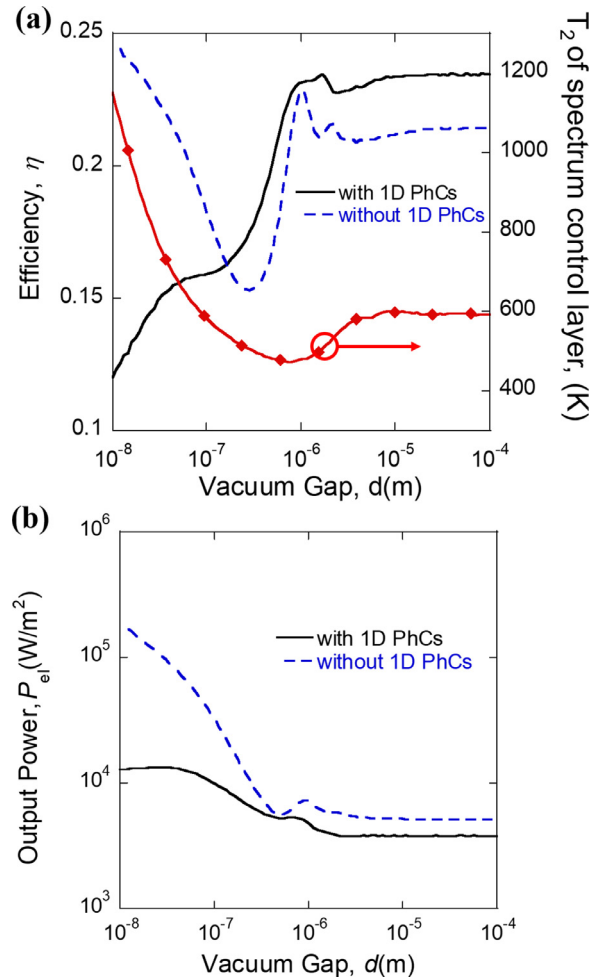
higher in Fig. 4(a) when $\lambda > 8\mu$m. Hence the ratio of energy transfer within the above-bandgap region to that for below-bandgap photons reduces. Subsequently, the efficiency of the three-body TPV system is much lower than that of conventional TPV counterparts at nanoscale gap distances, as shown in Fig. 3(a). Also, notice that $\xi_{1,2}(\omega, \beta) - \xi_{2,3}(\omega, \beta)$ increases as the vacuum gap shrinks, though not shown. To ensure the heat exchange between the emitter and intermediate layer is equal to that between intermediate layer and the receiver, the temperature difference $T_1 - T_2$ should be smaller than $T_2 - T_3$. That explains the temperature of the spectrum control layer is close to that of the emitter for nanoscale gap distances as shown in Fig. 3(a).

We can conclude from the above analyses that employing PhCs filters to improve the performance of TPV systems is not necessarily applicable to the near-field case. To achieve high performance in the near field, we chose a Drude model layer as the spectrum control layer. Generally, a Drude model can be given in the form $\varepsilon(\omega) = 1 - \omega_p^2/(\omega^2 + i\Gamma\omega)$[73], where Γ is the loss term and ω_p is the plasma frequency. Effects of ω_p and Γ on the efficiency and power output of the three-body near-field TPV system are given in Fig. 5 with $d = 10$ nm and $t = 10$ nm. As can be seen clearly, $\omega_p = 1.2 \times 10^{15}$ rad/s is a clear dividing line between a good performance (for both efficiency and output power) and a relatively bad one. In the range of $1.2 \times 10^{15} < \omega_p < 2.4 \times 10^{15}$ rad/s, the system has a conversion efficiency of more than 30% and an output power higher than 3×10^5W/m^2. The maximum efficiency we

(a)

(b)

(c)
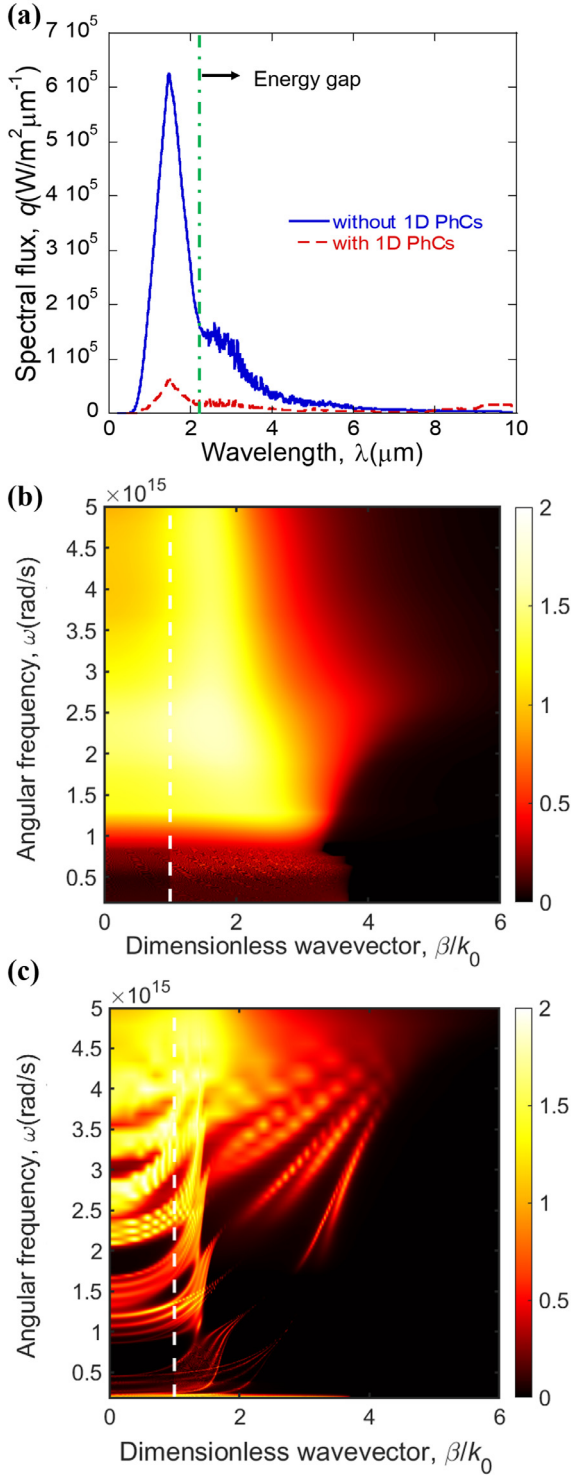
Fig. 4. Spectral heat flux of different TPV systems at $d = 10$ nm. The vertical green line represents bandgap at $\lambda = \lambda_g = 2.22\ \mu$m. (b) energy transmission coefficients $\xi(\omega, \beta)$ of the TPV system without 1D PhCs. (c) $\xi_{1,3}(\omega, \beta) + \xi_{2,3}(\omega, \beta)$ for the TPV system with 1D PhCs.

obtain is 35.3% at $\omega_p = 1.2 \times 10^{15}$ rad/s and $\Gamma = 2.9 \times 10^{12}$ rad/s. The maximum power of 3.62×10^5 W/m^2 is located at $\omega_p = 1.51 \times 10^{15}$ rad/s and $\Gamma = 7.01 \times 10^{13}$ rad/s. Although the maximum efficiency and power don't occur at the same point, obvious improvements of both efficiency and power are obtained for a broad region of both ω_p and Γ. When $\Gamma < 2 \times 10^{14}$ rad/s, η and P_{el} are not sen-

(a)

(b)
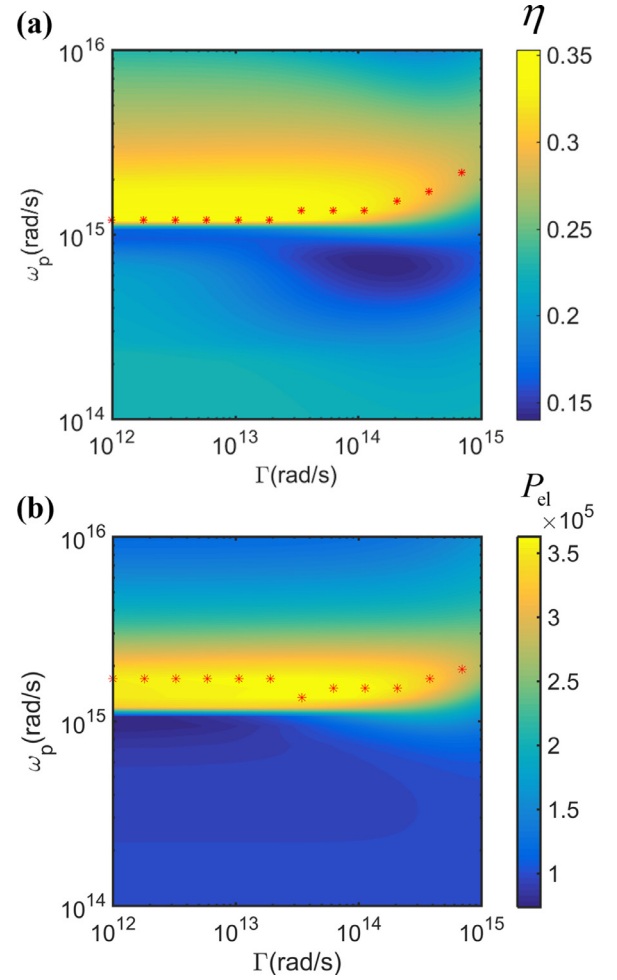
Fig. 5. Conversion efficiency η (a) and output power P_{el} (b) varying with dielectric function parameters of the thin spectrum control layer. The $*$ indicates the maximum of performance at each Γ.

sitive to the change of Γ. When Γ continues to increase beyond 2×10^{14} rad/s, η and P_{el} decrease evidently, and both of their maximums shift to a larger ω_p, as can be clearly seen in Fig. 5.

To better explain how dielectric parameters of the thin intermediate layer affect the efficiency and output power, three cases (Case 1: $\omega_p = 1.2 \times 10^{15}$ rad/s and $\Gamma = 2 \times 10^{13}$ rad/s; Case 2: $\omega_p = 2 \times 10^{15}$ rad/s and $\Gamma = 2 \times 10^{13}$ rad/s; Case 3: $\omega_p = 1.2 \times 10^{15}$ rad/s and $\Gamma = 5 \times 10^{14}$ rad/s) are taken as examples. Their spectral fluxes are given in Fig. 6. For Case 1, where the maximum efficiency point is located nearby, its radiation spectrum is mainly concentrated around $\lambda = 1.94\ \mu$m with a peak value of 3.8×10^6 W/m$^2\mu$m^{-1}. The excellent monochromaticity and high radiative flux in the $\lambda < \lambda_g$ art lead to a significant increase in the conversion efficiency and output power of the system. Keeping Γ as the same while increasing ω_p to 2×10^{15} rad/s(Case 2), it can be seen that the spectral flux within 1.2 μm $< \lambda < 2.2\ \mu$m is improved tremendously. Nevertheless, the peak value decreases by 68.7 percent, and thermalization losses increase due to the deteriorated monochromaticity, as a result, the efficiency decreases from 34.7% to 32.2%. If we only increase Γ to 5×10^{14} rad/s with ω_p remaining the same (Case 3), the peak location of spectral flux does not change but the peak value decreases tremendously to 8.6×10^5 W/m$^2\mu$m^{-1}. Besides, the full width at half maximum also becomes larger, and the spectral radiative flux below the bandgap has a prominent increase. That is why the efficiency has a sharp decrease from 34.7% to 23.4%.
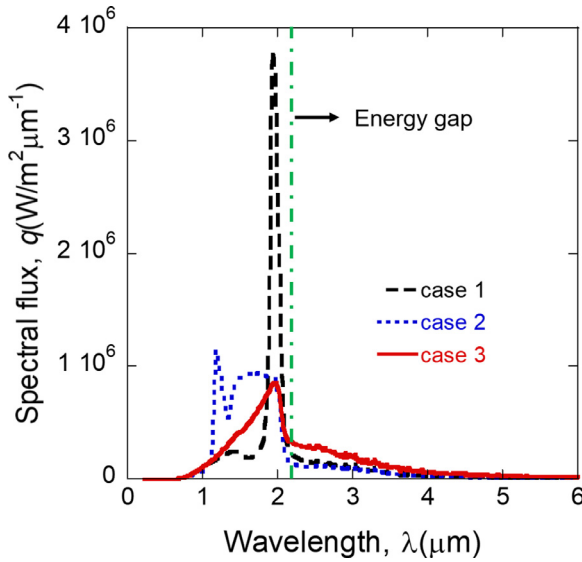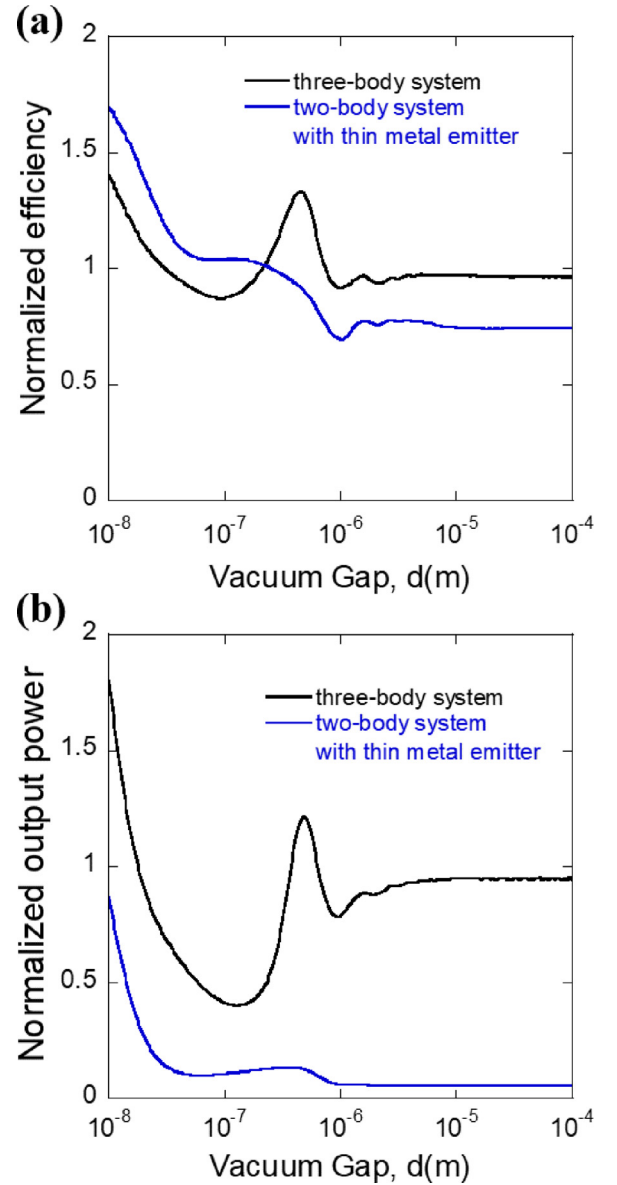
Fig. 6. Spectral heat flux of the three-body TPV system with different dielectric parameters of the spectrum control layer at $d = 10$ nm and $t = 10$ nm. Case 1:$\omega_p = 1.2 \times 10^{15}$ rad/s and $\Gamma = 2 \times 10^{13}$ rad/s; Case 2: $\omega_p = 2 \times 10^{15}$ rad/s and $\Gamma = 2 \times 10^{13}$ rad/s; Case 3: $\omega_p = 1.2 \times 10^{15}$ rad/s and $\Gamma = 5 \times 10^{14}$ rad/s. The vertical green line is at $\lambda=\lambda_g = 2.22$ μm.
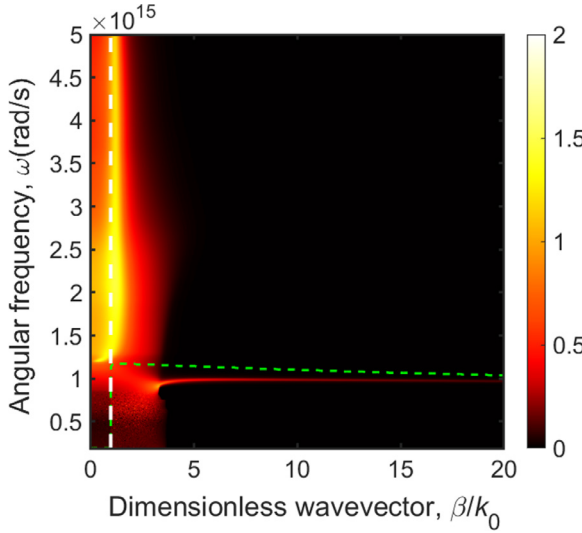
Fig. 7. Energy transmission coefficients $\xi_{1,3}(\omega, \beta) + \xi_{2,3}(\omega, \beta)$ for case 1, which is kept at $d = 10$ nm and $t = 10$ nm. White and green dotted lines represent light lines and the high-frequency asymmetric mode of the film's coupled SPPs in vacuum, respectively.

Fig. 8. (a) normalized efficiency, (b) normalized output power. Variation of the improvement performance for the case 1 system at $t = 10$ nm with the vacuum gap d, which are normalized by the conventional TPV system's performance without any spectrum control layer with its emitter and receiver separated by the same gap distance of d. Also, the normalized performance of the two-body system with an 10nm thin metal emitter(case 1) is shown for comparison.

Taking case 1 as an example, we draw the three-body system's energy transmission coefficients in Fig. 7 to reveal the spectrum control layer's enhancement mechanism. The energy transmission coefficient is the total of $\xi_{1,3}(\omega, \beta)$ and $\xi_{2,3}(\omega, \beta)$, which considers contributions to the receiver from the emitter and intermediate spectrum control layer, respectively. As can be clearly seen, there is a narrow region around $\omega = 9.74 \times 10^{14}$ rad/s featured with high energy transmission coefficients even at high wavevector values. The green dotted line is the high-frequency asymmetric mode of the film's coupled surface plasmon polarizations (SPPs) with a dispersion relationship of $\tanh(ik_{2z}t)(k_{2z}^2/\varepsilon_2^2 + k_z^2) - 2k_zk_{2z}/\varepsilon_2 = 0$ in the vacuum [73,74], where $k_z = \sqrt{(\omega/c0)^2 - \beta^2}$ and$k_{2z} = \sqrt{\varepsilon_2(\omega/c0)^2 - \beta^2}$. The agreement between the high energy transmission coefficient region with the green dotted line is very good, confirming the contribution of SPPs in enhancing radia-

tive heat transfer, especially for high wavevector modes. The excitation frequency $\omega = 9.74 \times 10^{14}$ rad/s($\lambda = 1.94$ μm) of SPPs coincides with the peak of spectral radiative heat flux as shown in Fig. 6, further confirming the dominant role of SPPs in enhancing radiative heat transfer and spectrum monochromaticity and thus improving energy conversion efficiency and output power of TPV systems.

In Fig. 8, we consider how the improvement performance of inserting a thin film(case 1) changes with the gap distance. As the gap distance increases, both the efficiency and output power normalized to those of two-body TPV systems decrease rapidly. This is not surprising considering that the coupling of SPPs with high-wavevector waves becomes weak at large gap distances. However, when the gap distance further increases beyond 130 nm, it is interesting to find that the system performance has a quick increase, and the efficiency and output power can increase by 30%
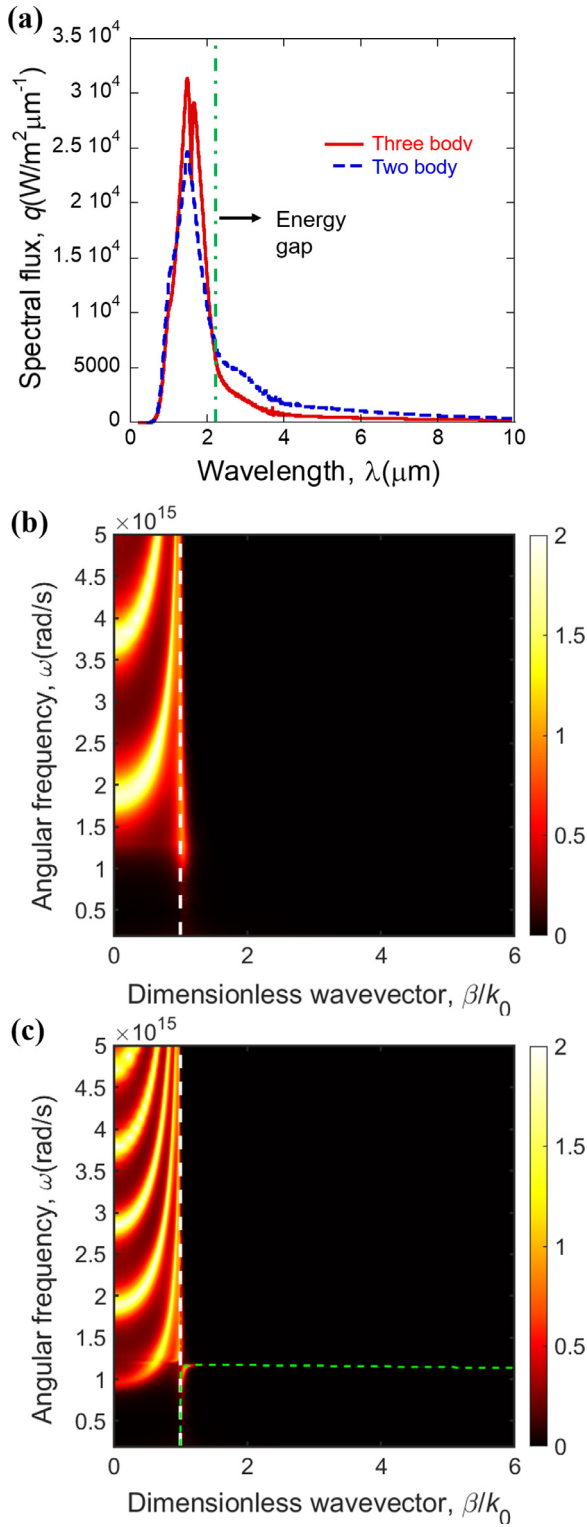
Fig. 9. (a) Spectral heat flux of different TPV systems, Case 1 parameters are used for the three-body system and $d = 483$ nm. (b) energy transmission coefficients $\xi(\omega, \beta)$ of the two-body system. (c) $\xi_{1,3}(\omega, \beta) + \xi_{2,3}(\omega, \beta)$ of the three-body system.

and 20% at 480 nm, respectively. For far-field cases, inserting the thin metallic layer slightly decreases the efficiency and output power by 3.5% and 5.5%, respectively. That is because the immediate layer can't excite the coupled SPPs and acts only as a thin radiation shield in the far-field.

To explain the reason why the system performance peaks around 480 nm, the spectral radiative flux is given in Fig. 9 (a). As we can see, the three-body system exhibit two adjacent peaks with high values of $3.14 \times 10^4 \mathrm{W/m^2 \mu m^{-1}}$ and $2.92 \times 10^4 \mathrm{W/m^2 \mu m^{-1}}$, respectively. The left peak is located at 1.46 μm, which is almost the same as that for the two-body system while its value is 29% higher. The additional peak is located at 1.64 μm. These two peaks increase the radiative heat flux greatly for the above-bandgap region, enabling a higher output power. To unveil the mechanism for the additional peak's presence, energy transmission coefficients are shown in Fig. 9(b) and Fig. 9(c) for two-body and three-body systems, respectively. Around $\omega = 1.15 \times 10^{15}$ rad/s, an additional bright region with high energy transmission coefficients outside the light line shows up. This can be attributed to the excitation of SPPs of the thin metallic layer, as can be confirmed from the excellent agreement with the dispersion relation of SPPs denoted as the green dotted line. And the reduction in the difference between the distributions of SPPs in the three-body system and the green curve also proves the attenuation of the three-body's coupled effect. Interestingly, this resonance makes the radiative heat flux drop more sharply across the bandgap, and the radiative transfer of below-bandgap photons is inhibited to some extent. That contributes to the improved conversion efficiency by 5.4%, as shown in Fig. 9(a).

Given an emitter that can support SPPs has great potential to improve a TPV system's performance [28,29,39], we have compared the three-body system's performance to that of the two-body system with a 10 nm thin metal emitter. The efficiency and output power normalized to those of the conventional tungsten-emitter two-body system are given in Fig. 8. As can be seen in Fig. 8(a), the two-body system with a thin metal emitter indeed exhibits a quite high efficiency in the near-field. However, as d increases, the efficiency decreases sharply and is lower than that of the three-body system when d is larger than 225 nm. As shown in Fig. 8(b), the output power of the two-body system with a thin metal emitter is much lower than that of the three-body system for the whole range of gap distance ranging from 10^{-8} m to 10^{-4} m. Such a low output power will make the advantage of near-field TPV system over traditional counterparts trivial. The near-field TPV system loses its traditional advantages. Therefore, the three-body system exhibits both moderate efficiencies and power output while the two-body system with a thin metal emitter has a low power output for a wide range of gap distances.

In this part, we will discuss the optimization of the position and thickness of the immediate Drude model layer. For the position optimization, the case 1 Drude model layer is used. When $d = 10$ nm, the total vacuum gap width is 20 nm. We take d_1 as the width the vacuum gap near the emitter, so the width of the vacuum gap near the PV cell is $d_2 = 20$ nm $- d_1$. As the d_1 increases, both the efficiency and output power increase and then decrease sharply. The optimal position is $d_1 = 12$ nm, corresponding to the maximum power $3.47 \times 10^5 \mathrm{W/m^2}$ and the maximum efficiency of 34.9%. However, as the total vacuum gap($2d$) increases, the rule no longer holds due to the weakened three-body coupled effect. For the thickness of the immediate metal, it has more complex effects on performance which is showed in Fig. 10. With Γ fixed at 2×10^{13} rad/s, we screen out the optimal thickness t at $d = 10$ nm. The three-body system's performance is superior in the area 1×10^{15} rad/s $< \omega_\mathrm{p} < 2 \times 10^{15}$ rad/s. This is because ω_spp is slightly larger than ω_g. Both $\eta_\mathrm{F}/\eta_\mathrm{c}$ and $P_\mathrm{elF}/P_\mathrm{elc}$ can obtain large values in the area of 10 nm $< t <$ 100 nm. The maximum output power can reach $6.08 \times 10^5 \mathrm{W/m^2}$ which is 2.2 times higher than the two-body system. However, in the region close to $t = 1$ μm, the efficiency can achieve greater value 43.9% and get a 70% improvement. This is because the distance between the emitter and the photovoltaic cell becomes very large, and the energy transmission coefficient except for surface plasma modes of the two bod-

(a)

(b)
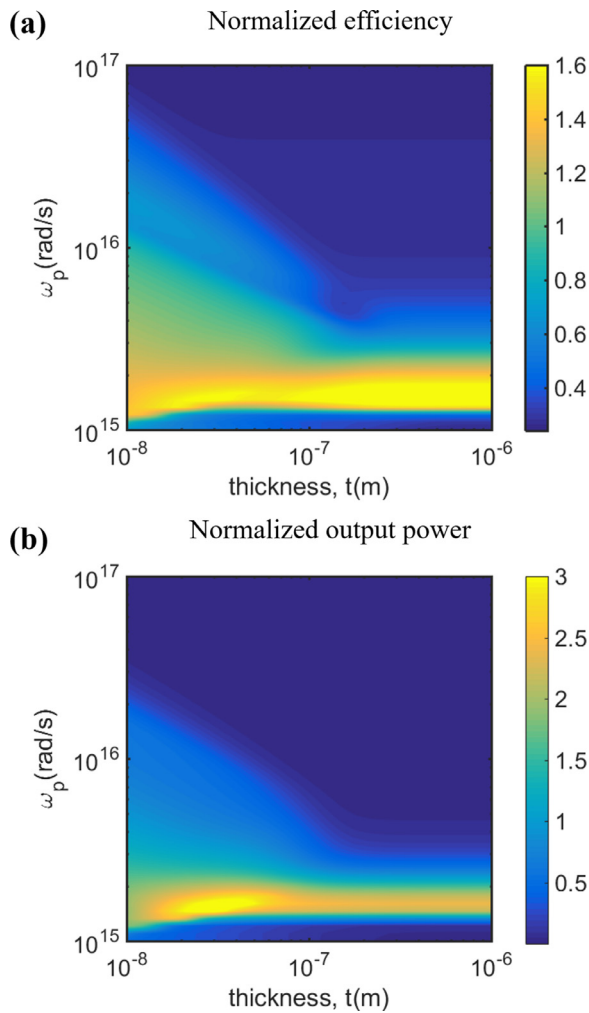
Fig. 10. (a) normalized conversion efficiency (b) normalized output power of the three-body system with a Drude model layer whose thickness varies from 10^{-8} m to 10^{-6} m and ω_p varies from 10^{15} rad/sto 10^{17} rad/sat $d = 10$ nm. The conventional TPV system without any spectrum control layer at $d = 10$ nm is used for comparison.

ies decreases sharply, significantly reducing the energy transfer of below-bandgap photons. At this time, the output power has decreased but it is still more than twice the power of ordinary thermal photovoltaic systems.

4. Conclusion

This paper investigates how inserting an intermediate spectrum control layer tunes the conversion efficiency and output power of near-field TPV systems based on dyadic Green function methods and fluctuation-dissipation theory. The temperature of the intermediate layer can be precisely obtained based on energy balance. It is found that inserting traditional photonic crystals may deteriorate both the conversion efficiency and power output of near-field TPV systems, although they help to improve system performance in the far field. By employing a thin metallic film as the spectrum control layer, the efficiency and output power at the gap distance of 10 nm can be enhanced from 24.7% and 1.88×10^5 W/m^2 to 35.3% and 3.62×10^5 W/m^2, respectively. Besides the deep near-field region, inserting this thin metallic film is also helpful around gap distance of half micron. The underlying mechanism is attributed to the excitation of surface plasmon polaritons. This work

provides new routes to further improve the performance of near-field thermophotovoltaic systems.

Declaration of Competing Interest

There are no conflicts of interest.

CRediT authorship contribution statement

Chunzhuo Dang: Software, Validation, Formal analysis, Investigation, Writing - original draft, Visualization. **Xianglei Liu:** Conceptualization, Resources, Writing - review & editing, Supervision, Funding acquisition, Project administration. **Haifeng Xia:** Methodology. **Shizheng Wen:** Data curation. **Qiao Xu:** Writing - review & editing.

References

[1] Zhao B, Chen K, Buddhiraju S, Bhatt G, Lipson M, Fan S. High-performance near-field thermophotovoltaics for waste heat recovery. Nano Energy 2017;41:344–50.

[2] Bright TJ, Wang LP, Zhang ZM. Performance of near-field thermophotovoltaic cells enhanced with a backside reflector. J Heat Transfer 2014;136(6):062701.

[3] Fitriani Ovik R, Long BD, Barma MC, Riaz M, Sabri MFM, et al. A review on nanostructures of high-temperature thermoelectric materials for waste heat recovery. Renewable Sustainable Energy Rev 2016;64:635–59.

[4] Fiorino A, Zhu L, Thompson D, Mittapally R, Reddy P, Meyhofer E. Nanogap near-field thermophotovoltaics. Nat Nanotechnol 2018;13:806–11.

[5] Watjen JI, Liu X, Zhao B, Zhang Z. A computational simulation of using tungsten gratings in near-field thermophotovoltaic devices. J Heat Transfer 2017;139(5):052704.

[6] Karalis A, Joannopoulos J. 'Squeezing'near-field thermal emission for ultra-efficient high-power thermophotovoltaic conversion. Sci Rep 2016;6:28472.

[7] Tervo E, Bagherisereshki E, Zhang Z. Near-field radiative thermoelectric energy converters: a review. Front Energy 2018;12:5–21.

[8] Mbakop FK, Djongyang N, Raïdandi D. One–dimensional TiO$_2$/SiO$_2$ photonic crystal filter for thermophotovoltaic applications. JEur Opt Soc-Rapid Pub 2016;12:23.

[9] O'Sullivan F, Celanovic I, Jovanovic N, Kassakian J, Akiyama S, Wada K. Optical characteristics of one-dimensional Si/SiO$_2$ photonic crystals for thermophotovoltaic applications. J Appl Phys 2005;97:033529.

[10] Celanovic I, O'Sullivan F, Ilak M, Kassakian J, Perreault D. Design and optimization of one-dimensional photonic crystals for thermophotovoltaic applications. Opt Lett 2004;29:863–5.

[11] Liu G, Xuan Y, Han Y, Li Q. Investigation of one-dimensional Si/SiO 2 hotonic crystals for thermophotovoltaic filter. Sci China Ser E: Technol Sci 2008;51:2031–9.

[12] Nelson RE. A brief history of thermophotovoltaic development. Semicond Sci Technol 2003;18:S141.

[13] DePoy DM, Fourspring PM, Ehsani H, Lazo-Wasem JE, Gratrix EJ. Development of front surface, spectral control filters with greater temperature stability for thermophotovoltaic energy conversion. In: AIP conference proceedings. American Institute of Physics; 2007. p. 59–67.

[14] Woolf DN, Kadlec EA, Bethke D, Grine AD, Nogan JJ, Cederberg JG, et al. High-efficiency thermophotovoltaic energy conversion enabled by a metamaterial selective emitter. Optica 2018;5:213–18.

[15] Baldasaro P, Raynolds J, Charache G, DePoy D, Ballinger C, Donovan T, et al. Thermodynamic analysis of thermophotovoltaic efficiency and power density tradeoffs. J Appl Phys 2001;89:3319–27.

[16] Fu C, Zhang Z. Nanoscale radiation heat transfer for silicon at different doping levels. Int J Heat Mass Transfer 2006;49:1703–18.

[17] Park K, Basu S, King WP, Zhang ZM. Performance analysis of near-field thermophotovoltaic devices considering absorption distribution. J Quant Spectrosc Radiat Transfer 2008;109:305–16.

[18] Polder D, Van Hove M. Theory of radiative heat transfer between closely spaced bodies. Phys Rev B 1971;4:3303.

[19] Liu X, Wang L, Zhang ZM. Near-field thermal radiation: recent progress and outlook. Nanoscale Microscale Thermophys Eng 2015;19:98–126.

[20] St-Gelais R, Zhu L, Fan S, Lipson M. Near-field radiative heat transfer between parallel structures in the deep subwavelength regime. Nat Nanotechnol 2016;11:515–19.

[21] Wen S, Liu X, Cheng S, Wang Z, Zhang S, Dang C. Ultrahigh thermal rectification based on near-field thermal radiation between dissimilar nanoparticles. J Quant Spectrosc Radiat Transfer 2019;234:1–9.

[22] Tervo EJ, Cola BA, Zhang ZM. Comparison of kinetic theory and fluctuational electrodynamics for radiative heat transfer in nanoparticle chains. J Quant Spectrosc Radiat Transfer 2020;246:106947.

[23] Czapla B, Narayanaswamy A. Thermal radiative energy exchange between a closely-spaced linear chain of spheres and its environment. J Quant Spectrosc Radiat Transfer 2019;227:4–11.

[24] Chen M, He Y, Hu Y, Zhu J. Local temperature control of hybrid plasmonic nano-antennas. J Quant Spectrosc Radiat Transfer 2019;225:50–7.

[25] Song J, Cheng Q. Near-field radiative heat transfer between graphene and anisotropic magneto-dielectric hyperbolic metamaterials. Phys Rev B 2016;94(12):125419.

[26] Luo M, Zhao J, Liu L. Near-field radiative heat transfer in a chain of nanoparticles with another chain in proximity. J Quant Spectrosc Radiat Transfer 2020;243:106801.

[27] Wang H, Chen K, Pan J, Huang S, Lin J, Xie W, et al. Modified plasmonic response of dimer nanoantennas with nonlocal effects: From near-field enhancement to optical force. J Quant Spectrosc Radiat Transfer 2020;245:106878.

[28] Ilic O, Jablan M, Joannopoulos JD, Celanovic I, Soljačić M. Overcoming the black body limit in plasmonic and graphene near-field thermophotovoltaic systems. Opt Express 2012;20:A366.

[29] Messina R, Ben-Abdallah P. Graphene-based photovoltaic cells for near-field thermal energy conversion. Sci Rep 2013;3:1–5.

[30] Pan JL, Choy HK, Fonstad C. Very large radiative transfer over small distances from a black body for thermophotovoltaic applications. IEEE Trans Electron Devices 2000;47:241–9.

[31] Laroche M, Carminati R, Greffet J-J. Near-field thermophotovoltaic energy conversion. J Appl Phys 2006;100:063704.

[32] Francoeur M, Vaillon R, Mengüç MP. Thermal impacts on the performance of nanoscale-gap thermophotovoltaic power generators. IEEE Trans Energy Convers 2011;26:686–98.

[33] Vongsoasup N, Francoeur M, Hanamura K. Performance analysis of near-field thermophotovoltaic system with 2D grating tungsten radiator. Int J Heat Mass Transfer 2017;115:326–32.

[34] Lim M, Jin S, Lee SS, Lee BJ. Graphene-assisted Si-InSb thermophotovoltaic system for low temperature applications. Opt Express 2015;23:A240–AA53.

[35] Lim M, Lee SS, Lee BJ. Effects of multilayered graphene on the performance of near-field thermophotovoltaic system at longer vacuum gap distances. J Quant Spectrosc Radiat Transfer 2017;197:84–94.

[36] Guo Y, Jacob Z. Thermal hyperbolic metamaterials. Opt Express 2013;21:15014–19.

[37] Whale M, Cravalho EG. Modeling and performance of microscale thermophotovoltaic energy conversion devices. IEEE Trans Energy Convers 2002;17:130–42.

[38] Whale MD. A fluctuational electrodynamic analysis of microscale radiative transfer and the design of microscale thermophotovoltaic devices. Massachusetts Institute of Technology; 1997.

[39] Narayanaswamy A, Chen G. Surface modes for near field thermophotovoltaics. Appl Phys Lett 2003;82:3544–6.

[40] Sabbaghi P, Yang Y, Chang J-Y, Wang L. Near-field thermophotovoltaic energy conversion by excitation of magnetic polariton inside nanometric vacuum gaps with nanostructured Drude emitter and backside reflector. J Quant Spectrosc Radiat Transfer 2019;234:108–14.

[41] Zhou C, Zhang Y, Qu L, Yi H-L. Near-field negative electroluminescent cooling via nanoparticle doping. J Quant Spectrosc Radiat Transfer 2020;245:106889.

[42] DiMatteo RS, Greiff P, Finberg SL, Young-Waithe KA, Choy H, Masaki MM, et al. Enhanced photogeneration of carriers in a semiconductor via coupling across a nonisothermal nanoscale vacuum gap. Appl Phys Lett 2001;79:1894–6.

[43] DiMatteo R, Greiff P, Seltzer D, Meulenberg D, Brown E, Carlen E, et al. Micron-gapT hermo P hoto V oltaics (MTPV). In: AIP conference proceedings. American Institute of Physics; 2004. p. 42–51.

[44] Hanamura K, Mori K. Nano-gap TPV generation of electricity through evanescent wave in near-field above emitter surface. AIP conference proceedings2007. p. 291–6.

[45] Bhatt GR, Zhao B, Roberts S, Datta I, Mohanty A, Lin T, et al. Integrated near–field thermo-photovoltaics for heat recycling. Nat Commun 2020;11:1–7.

[46] Tong JK, Hsu WC, Huang Y, Boriskina SV, Chen G. Thin-film 'Thermal well' emitters and absorbers for high-efficiency thermophotovoltaics. Sci Rep 2015;5:10661.

[47] Jin S, Lim M, Lee SS, Lee BJ. Hyperbolic metamaterial-based near-field thermophotovoltaic system for hundreds of nanometer vacuum gap. Opt Express 2016;24:A635.

[48] Lim M, Song J, Kim J, Lee SS, Lee I, Lee BJ. Optimization of a near-field thermophotovoltaic system operating at low temperature and large vacuum gap. J Quant Spectrosc Radiat Transfer 2018;210:35–43.

[49] Shi J, Liu B, Li P, Ng LY, Shen S. Near-field energy extraction with hyperbolic metamaterials. Nano Lett 2015;15:1217–21.

[50] Wang H, Dong Q. Wideband absorption enhancement analysis of doped silicon nanocone arrays based on anisotropic effective medium approximation. International heat transfer conference digital library. Begel House Inc; 2018.

[51] Messina R, Antezza M, Ben-Abdallah P. Three-body amplification of photon heat tunneling. Phys Rev Lett 2012;109:244302.

[52] He M-J, Qi H, Li Y, Ren Y-T, Cai W-H, Ruan L-M. Graphene-mediated near field thermostat based on three-body photon tunneling. Int J Heat Mass Transfer 2019;137:12–19.

[53] Ben-Abdallah P, Biehs S-A. Near-field thermal transistor. Phys Rev Lett 2014;112:044301.

[54] Wang L, Zhang Z. Thermal rectification enabled by near-field radiative heat transfer between intrinsic silicon and a dissimilar material. Nanoscale Microscale Thermophys Eng 2013;17:337–48.

[55] Zheng Z, Xuan Y. Enhancement or suppression of the near-field radiative heat transfer between two materials. Nanoscale Microscale Thermophys Eng 2011;15:237–51.

[56] Kan YH, Zhao CY, Zhang ZM. Near-field radiative heat transfer in three-body systems with periodic structures. Phys Rev B 2019;99:035433.

[57] Joulain K, Ezzahri Y, Drevillon J, Ben-Abdallah P. Modulation and amplification of radiative far field heat transfer: towards a simple radiative thermal transistor. Appl Phys Lett 2015;106:133505.

[58] Latella I, Pérez-Madrid A, Rubi JM, Biehs S-A, Ben-Abdallah P. Heat engine driven by photon tunneling in many-body systems. Phys Rev Appl 2015;4:011001.

[59] Prod'homme H, Ordonez-Miranda J, Ezzahri Y, Drévillon J, Joulain K. VO2-based radiative thermal transistor with a semi-transparent base. J Quant Spectrosc Radiat Transfer 2018;210:52–61.

[60] Gu W, Tang G-H, Tao W-Q. Thermal switch and thermal rectification enabled by near-field radiative heat transfer between three slabs. Int J Heat Mass Transfer 2015;82:429–34.

[61] Liu X, Zhang ZM. High-performance electroluminescent refrigeration enabled by photon tunneling. Nano Energy 2016;26:353–9.

[62] Palik ED. Handbook of optical constants of solids. Academic Press; 1998.

[63] González-Cuevas JA, Refaat TF, Abedin MN. Elsayed-Ali HE. Modeling of the temperature-dependent spectral response of in $1-\chi$ ga χ sb infrared photodetectors. Opt Eng 2006;45:044001.

[64] Rytov S, Kravtsov YA, Tatarskii V. Principles of statistical radiophysics. Vol. 4, wave propagation 1989.

[65] Sipe JE. New Green-function formalism for surface optics. JOSA B 1987;4:481–9.

[66] Francoeur M, Mengüç MP, Vaillon R. Solution of near-field thermal radiation in one-dimensional layered media using dyadic Green's functions and the scattering matrix method. J Quant Spectrosc Radiat Transfer 2009;110:2002–18.

[67] Narayanaswamy A, Chen G. Thermal emission control with one-dimensional metallodielectric photonic crystals. Phys Rev B 2004;70:125101.

[68] Narayanaswamy A, Chen G. Thermal radiation in 1D photonic crystals. J Quant Spectrosc Radiat Transfer 2005;93:175–83.

[69] Chang J-Y, Yang Y, Wang L. Tungsten nanowire based hyperbolic metamaterial emitters for near-field thermophotovoltaic applications. Int J Heat Mass Transfer 2015;87:237–47.

[70] Feng D, Tervo EJ, Yee SK, Zhang ZM. Effect of evanescent waves on the dark current of thermophotovoltaic cells. Nanoscale Microscale Thermophys Eng 2020;24:1–19.

[71] Ashcroft N, Mermin N. Solid state physics saunders; 1976. New York p. 22.

[72] Chen D-ZA, Chen G. Measurement of silicon dioxide surface phonon-polariton propagation length by attenuated total reflection. Appl Phys Lett 2007:91.

[73] Zhang ZM. Nano/microscale heat transfer. New York: McGraw-Hill; 2007.

[74] Economou EN. Surface Plasmons in Thin Films. Phys Rev 1969;182:539–54.